ACS APPLIED MATERIALS & INTERFACES

Research Article

www.acsami.org

Carrier Step-by-Step Transport Initiated by Precise Defect Distribution Engineering for Efficient Photocatalytic Hydrogen Generation

Jiewei Chen,[†] Gaoxiang Wu,[†] Tianyue Wang,[†] Xiaodan Li,[†] Meicheng Li,[*,†,‡] Yuanhua Sang,[§] and Hong Liu[§]

[†]State Key Laboratory of Alternate Electrical Power System with Renewable Energy Sources, North China Electric Power University, Beijing 102206, China

[‡]Chongqing Materials Research Institute, Chongqing 400707, China

[§]State Key Laboratory of Crystal Materials, Shandong University, Jinan 250100, China

Supporting Information

ABSTRACT: Semiconductor photocatalysts have been widely used for solar-to-hydrogen conversion; however, efficient photocatalytic hydrogen generation still remains a challenge. To improve the photocatalytic activity, the critical step is the transport of photogenerated carriers from bulk to surface. Here, we report the carrier step-by-step transport (CST) for semiconductor photocatalysts through precise defect engineering. In CST, carriers can fast transport from bulk to shallow traps in the defective subsurface first, and then transfer to the surface active acceptors. The key challenge of initiating CST lies in fine controlling defect distribution in semiconductor photocatalysts to introduce the special band matching between the crystalline bulk and defect-controllable surface, moderate bridgelike shallow traps induced by subsurface defects, and abundant surface active sites induced by surface defects. In our proof-of-concept demonstration, the CST was introduced into typical semiconductor TiO_2 assisted by the fluorine-assisted kinetic hydrolysis method, and the designed TiO_2 can exhibit the state-of-the-art photocatalytic hydrogen generation rate among anatase TiO_2 up to 13.21 mmol h^{-1} g^{-1}, which is 120 times enhanced compared with crystalline anatase TiO_2 under sunlight. The CST initiated by precise defect distribution engineering provides a new sight on greatly improving photocatalytic hydrogen generation performance of semiconductor catalysts.

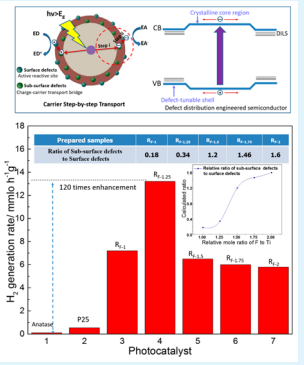

KEYWORDS: *carrier step-by-step transport, precise defect distribution engineering, photocatalytic hydrogen generation, special band matching, bridgelike shallow traps, surface active acceptors*

1. INTRODUCTION

Semiconductor photocatalysis plays an important role in converting the abundant, and safe solar power into clean energy such as hydrogen, which leads a major advance in the sustainable development of society.[1−5] To design effective semiconductor photocatalysts for hydrogen generation reaction, there are three fundamental factors: enough light absorption, active light-driven surface reactivity, and efficient carrier transport to the surface.[1,2,6−10] Tremendous efforts have been made to improve the light absorption[11,12] (e.g., doping nonmetal ions[13]) and enhance the surface reactivity[3] (e.g., introducing active reactive sits[14]); however, efficiently facilitating carriers transport from bulk to surface still remains challenging because the transport of carriers is intrinsically sensitive to the crystal structures of the materials.

To promote the transport kinetics of carriers for efficient photocatalytic hydrogen generation, the unique carrier transport is proposed in semiconductor photocatalysts (Figure 1). Such a transport is based on constructing three elements simultaneously: (i) the special band alignment, (ii) bridgelike shallow traps induced by moderate subsurface defects and (iii) active carrier acceptors induced by abundant surface defects by fine defect distribution engineering. Through the special band matching between the crystalline core and the defective shell, after photoexcitation, both electrons and holes can easily transport from bulk to surface. Moreover, moderate subsurface defects can induce the shallow traps of carriers, acting as the transport bridge of carriers between bulk and surface. Furthermore, abundant surface defects are introduced act as the active reactive sites to enhance the surface accepting ability of carriers. Hence, compared with the traditional one-step carrier transport in crystalline semiconductor (Figure 1a), this dynamic transport in designed defective semiconductor (Figure 1b) can be defined as "carrier step-by-step transport" (CST) for efficient photocatalytic hydrogen generation. In our proof-of-concept, the CST was introduced into typical semiconductor

Received: November 17, 2016
Accepted: January 13, 2017
Published: January 13, 2017

DOI: 10.1021/acsami.6b14700
ACS Appl. Mater. Interfaces 2017, 9, 4634−4642

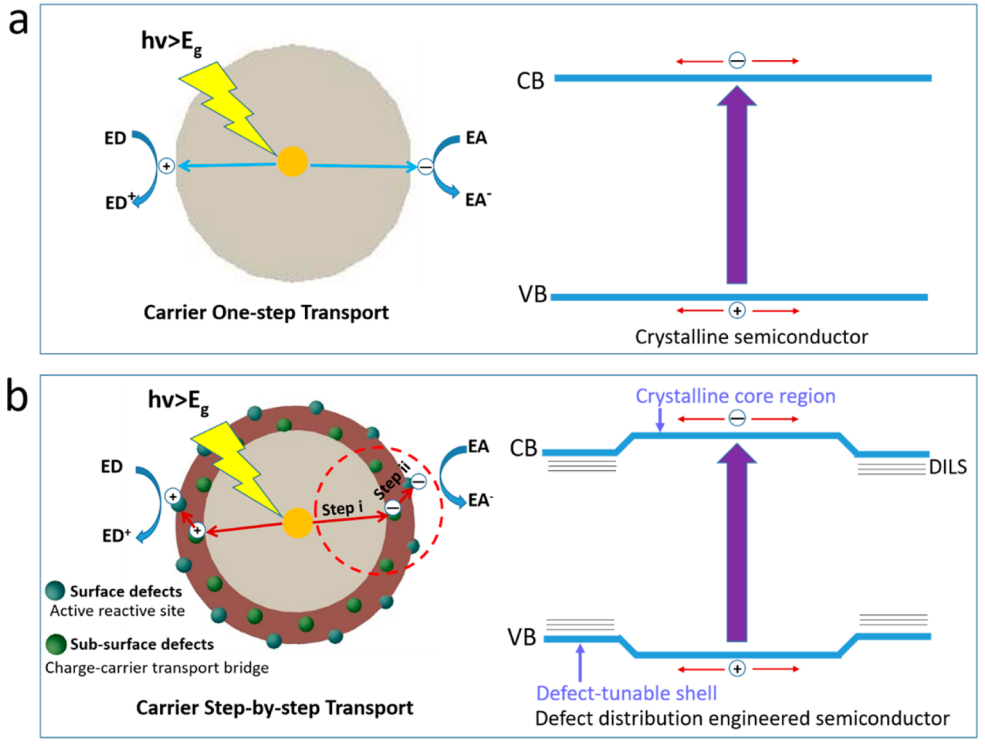

Figure 1. Different transport modes of carriers for photocatalysis in crystalline and defect-engineered semiconductors. (a) Carrier one-step transport in crystalline semiconductor. (b) Carrier step-by-step transport in defect-engineered semiconductor for efficient photocatalysis. EA, electron acceptor; ED, electron donor; CB, conduction band; VB, valence band; DILS, defect induced localized states.

photocatalyst TiO_2, and it exhibits the state-of-the-art photocatalytic hydrogen generation rate among anatase TiO_2 up to 13.21 mmol h^{-1} g^{-1} under solar light, which is 120 times enhanced than the crystalline anatase TiO_2.

2. EXPERIMENTAL SECTION

2.1. Materials Preparation. All of the chemical reagents of analytical grade were purchased from Shanghai Aladdin Bio-Chem Technology Co. and used as received without further purification. In a typical experiment, 2 mL of aqueous TBOT precursor was dissolved in 25 mL of n-propanol and then 0.8 mL of HF was added to the mixed solution (the relative raw material mole ratio of F:Ti ≈ 4:1). After the 2 h stirring, the obtained suspension was transferred to a Telfon-lined stainless steel autoclave and then heated at 180 °C for 18 h. After the reaction, the obtained product was washed with deionized water, and then was washed with alcohol (EtOH) and deionized water again. To identify different prepared samples, we marked the sample as "$R_{F\text{-}X}$" (F means the surfactant is HF, and X is the raw material mole ratio of F:Ti). In a control experiment, the reference sample TiO_2 with only Ti^{3+}_{surf} was prepared by using HF to treat the commercial anatase TiO_2 (~25 nm) and the sample TiO_2 with only $Ti^{3+}_{sub-surf}$ was prepared by heating $R_{F\text{-}4}$ in air for 2 h at 450 °C.

2.2. Materials Characterization. The morphology of the synthesized TiO_2 nanostructure was observed by FEI Quanta 200F microscope field emission scanning electron microscope (FESEM) and Tecnai G2 F20 field-emission transmission electron microscopy (TEM) with accelerating voltage of 200 kV. The crystalline phase was identified by a Bruker D8 Focus X-ray powder diffractometer using Cu K_α (λ = 1.5406 Å) radiation over a range of 2θ from 20° to 80°. Brunauer–Emmett–Teller (BET) surface areas of the samples were analyzed by nitrogen adsorption–desorption measurement on a Quantachrome Autosorb-IQ-MP sorption analyzer with prior degassing under vacuum at 77K. Pore size distribution was derived from desorption branch by a BJH method. EPR spectra were collected for powder samples on a Bruker Elexys E500 spectrometer at the frequency of 9.444 GHz at the Bruker Biospin Corporation at 90K. X-ray photoelectron spectrum (XPS) analysis was conducted with a ESCALAB 250Xi X-ray photoelectron spectroscope equipped with Al Kα radiation, and the binding energy was calibrated by the C 1s peak (284.8 eV) of contamination carbon. Time-of-flight secondary ion mass spectrometry (TOF-SIMS) was conducted using Cs^+ for sputtering (45°), with the speed of 0.071 nm/s. Photoluminescence (PL) spectra and PL decay profiles of samples were measured through the Edinburg Instruments FLS920 spectrofluorometer at room temperature with a 450 W xenon lamp. The PL spectra were measured at the excitation of 350 nm. The PL decay profile were measured using a 375 nm nanosecond laser and the detection wavelength of the emission is 430 nm.

2.3. Photocatalysis Evaluation. *Photocatalytic Degrading Methyl Orange.* In a typical experiment, the catalyst sample of 100 mg was suspended in 100 mL of the 2×10^{-5} mol/L aqueous solution of methyl orange in the reaction cell. After a 0.5 h stirring under dark condition for adsorption and desorption with methyl orange, the reactor cell was irradiated with the optical filter AM1.5 (100 mW cm^{-2}). The blank experiment in the absence of catalyst was also performed as a control. Our prepared samples were washed with NaOH solution to remove the adsorbent fluorine before reaction to eliminate the surface fluorine referring to some works.[15,16] Total concentrations of dye aqueous solution were simply determined by the maximum absorption (~463 nm) measurements by UV–vis spectra. C/C_0 was used to describe the degradation efficiency that stands for the concentration ratio before and after a certain period of reaction time.

Photocatalytic Hydrogen Generation from Water Splitting. Photocatalytic hydrogen generation reactions were carried out in a top-irradiation-type Pyrex reaction cell connected to a closed glass gas-circulation and evacuation system under the irradiation of 300 W Xe lamp (Beijing Trusttech Co. Ltd., PLS-SXE-300UV) with the filter AM1.5 (100 mw cm^{-2}). In a typical experiment, 100 mg of the photocatalyst powder was dispersed in a 100 mL aqueous solution containing 20 mL methanol. For all TiO_2 samples, 1 wt % Pt was in situ photodeposited from 1 M H_2PtCl_6 aqueous solution as cocatalyst. The reaction temperature was kept around 293 K. The amount of H_2

DOI: 10.1021/acsami.6b14700
ACS Appl. Mater. Interfaces 2017, 9, 4634–4642

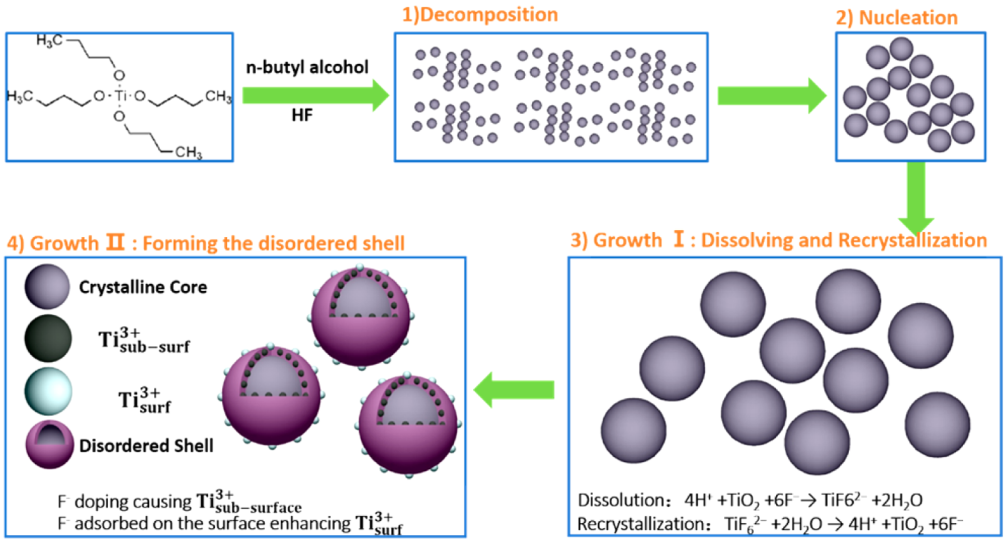

Figure 2. Formation process of defective TiO_2. Schematic illustration of the proposed fluorine-assisted hydrolysis mechanism in the forming process of the prepared defective TiO_2.

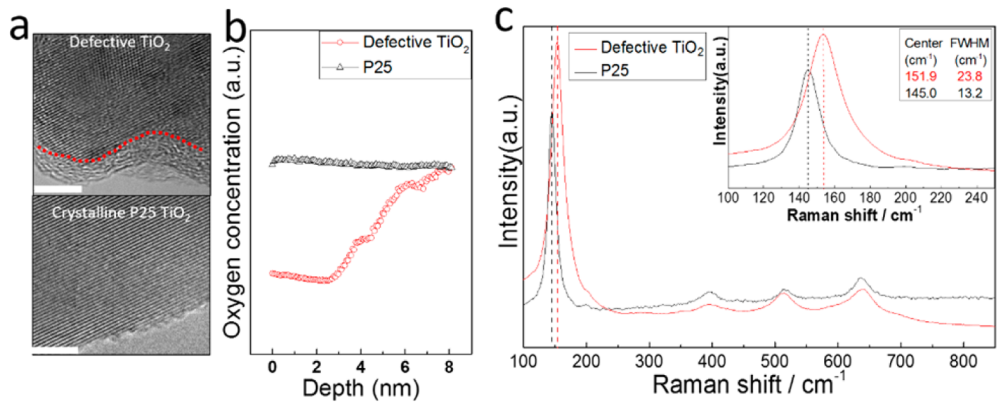

Figure 3. Characterization of the disordered shell/crystalline core structure of defective TiO_2 ($R_{F\text{-}4}$). (a) High-resolution transmission electron microscopy image of defective TiO_2 ($R_{F\text{-}4}$) compared with crystalline P25 (scale bar 5 nm). (b) TOF-SIMS depth profiles of oxygen concentration in synthesized TiO_2 ($R_{F\text{-}4}$) and P25. (c) Raman scattering spectra comparing defective TiO_2 ($R_{F\text{-}4}$).with crystalline P25. The inset: the most intense E_g peak of anatase TiO_2, along with corresponding peak center positions and widths.

generated was determined using a gas chromatograph (Beijing Trusttech Co. Ltd., GC-7920).

Apparent quantum efficiency (AQE) of H_2 evolution was conducted under the same photocatalytic condition. The 380 and 420 nm band-pass filters were used.

$$\mathrm{AQE} = \frac{\text{no. of reacted electrons}}{\text{no. of incident photons}} 100\% = \frac{2(\text{no. of evolved } H_2 \text{ molecules})}{\text{no. of incident photons}} 100\%$$

3. RESULTS AND DISCUSSION

The challenge of initiating the CST for TiO_2 lies in surrounding a crystalline core with the controllably defect-tailored shell in order to realize matching the band, importing moderate shallow traps and incorporating abundant surface active sites simultaneously. To synthesize TiO_2 with the crystalline core/defective shell structure, there are many reported harsh synthetic methods such as hydrothermal method,[6,17,18] Al-reduction,[19,20] hydrogen plasma,[21] and electrochemical reduction.[22] However, it still remains hard to controllably tailor the defect distribution in TiO_2 to simultaneously induce suitable band matching, moderate midgap states and abundant surface defects to initiate our design of the CST. Hence, to achieve our design, it is significant to propose a feasible method to controllably tailor the defect distribution. Because many works reported that fluorine plays an important role in synthesizing defective TiO_2,[23−26] we have considered taking advantage of the effects of fluorine on inducing and controlling the defects in TiO_2.

To initiate the CST, a fluorine-assisted dynamic solvothermal method was developed to achieve a crystalline core surrounded with the defect-tailored shell in TiO_2, as shown in Figure 2. In order to controllably tailor the defect distribution in TiO_2, we have clarified its forming mechanism by studying the affective factors on the reaction process (Section 1, Figure S1−S3), which suggests that it is a "fluorine-assisted dynamic solvothermal mechanism". It should be emphasized that the relatively much higher mole ratio of the solvent than the precursor and surfactant can not only ensure the formation of defective TiO_2 nanoparticles but also make it easier for the defect-control synthesis. To identify different prepared samples, hereafter we marked the sample as "$R_{F\text{-}X}$" (F means the surfactant is HF, and X is the raw material mole ratio of F:Ti).

DOI: 10.1021/acsami.6b14700
ACS Appl. Mater. Interfaces 2017, 9, 4634−4642

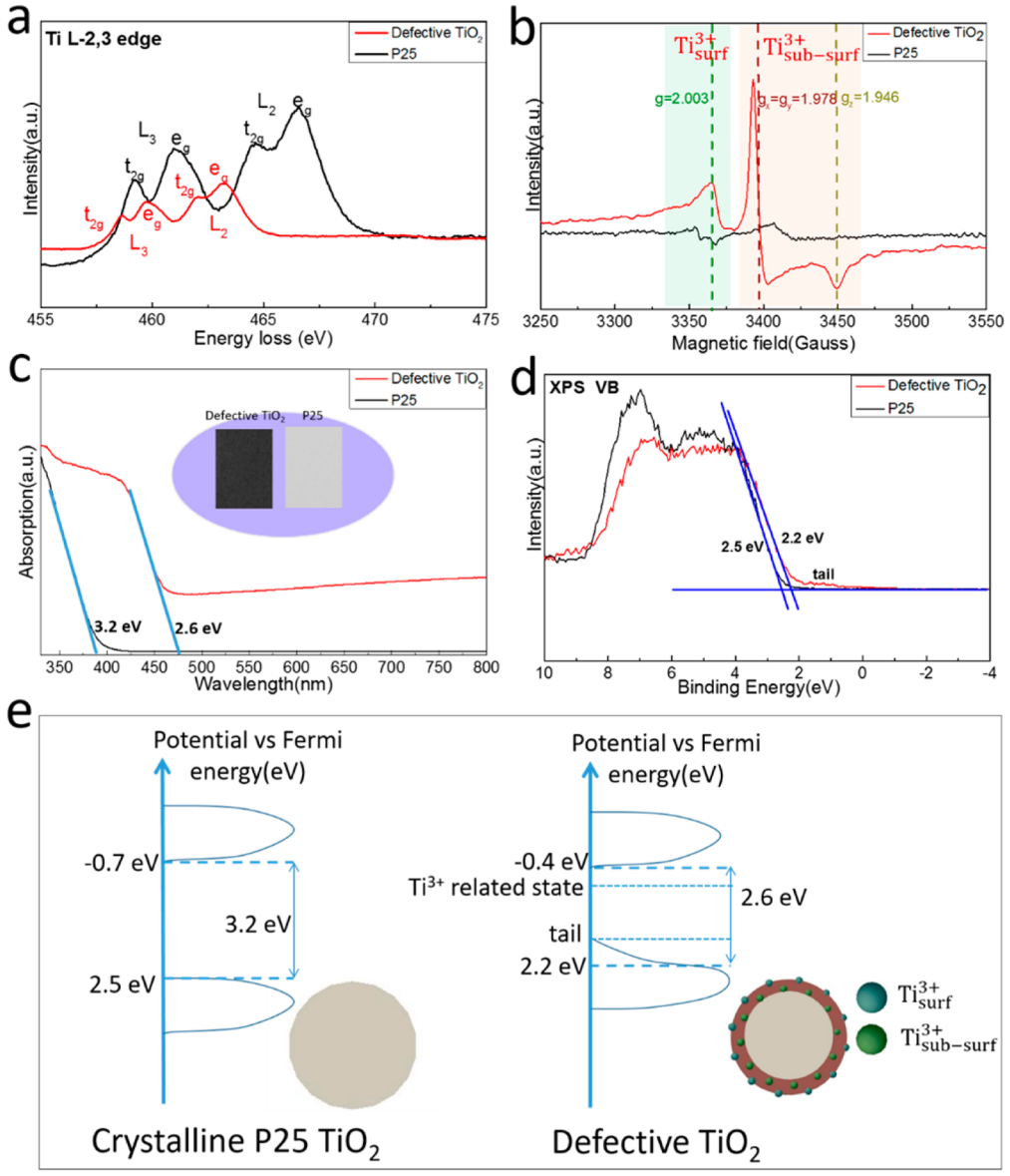

Figure 4. Detection of Ti^{3+} defects and the defect-induced energy band structure of defective TiO_2 (R_{F-4}) compared with crystalline P25 TiO_2. (a) Electron energy loss spectra of prepared defective TiO_2 and P25. (b) Electron paramagnetic resonance spectra of defective TiO_2 compared with P25. (c) Diffusive reflectance UV−vis spectra of prepared defective TiO_2 and P25. The inset: the photo of prepared defective TiO_2 comparing to P25. (d) Valence band spectra of defective TiO_2 and P25 from X-ray photoelectron. (e) Schematic illustration of the structure and the density of state for prepared defective TiO_2 and P25 TiO_2.

The morphology and structure of prepared defective TiO_2 (R_{F-4}) have been characterized. The X-ray diffraction (XRD) spectrum (Figure S4) indicates that the prepared TiO_2 is highly crystallized with the anatase phase (JCPDS No.21−1272). The scanning electron microscopy (SEM) image (the inset of Figure S4) shows the prepared TiO_2 is nanosheet like. And the transmission electron microscopy (TEM) observation (the inset in Figure S4) shows that the size of defective TiO_2 is about 25 nm. Brunauer−Emmett−Teller (BET) nitrogen adsorption−desorption analysis is conducted to present the textural properties of the prepared defective TiO_2 is shown in Figure S5. The HRTEM (Figure 2a) indicates that there is a crystalline core surrounded by a defective shell (~3 nm) in defective TiO_2 while P25 is nearly completely crystalline. To confirm that there is really a defective shell layer, we have carried out the TOF-SIMS test of prepared TiO_2 R_{F-4} (Figure 2b), which reveals that there is ~3 nm disordered layer outside the crystalline core because the concentration of O increases from steeply after about 3 nm ion etching.

The structure of the defective TiO_2 is further analyzed by Raman scattering, as shown in Figure 3c. The six ($3E_g$ + $2B1_g$ + $A1_g$) Raman-active modes of anatase phase are detected in investigated samples. The large blue-shift and broadening of the peak (the inset of Figure 3c) observed in defective TiO_2 compared with Degussa P25 TiO_2 indicate phonon confinement effects, which can be caused by finite-size effects (<10 nm) or the existence of the disorder defects.[6,27] Here, the size of defective TiO_2 (~25 nm) is much larger than 10 nm, ruling out the occurrence of finite-size effects resulting from the case of the small size of the grains. Hence, it is proposed that the defects in the disorder shell of defective TiO_2 cause the phonon confinement effects in prepared defective TiO_2. The XPS survey spectrum (Figure S6) shows there are both physically adsorbed and doping F in defective TiO_2,[23−25] which may

DOI: 10.1021/acsami.6b14700
ACS Appl. Mater. Interfaces 2017, 9, 4634−4642

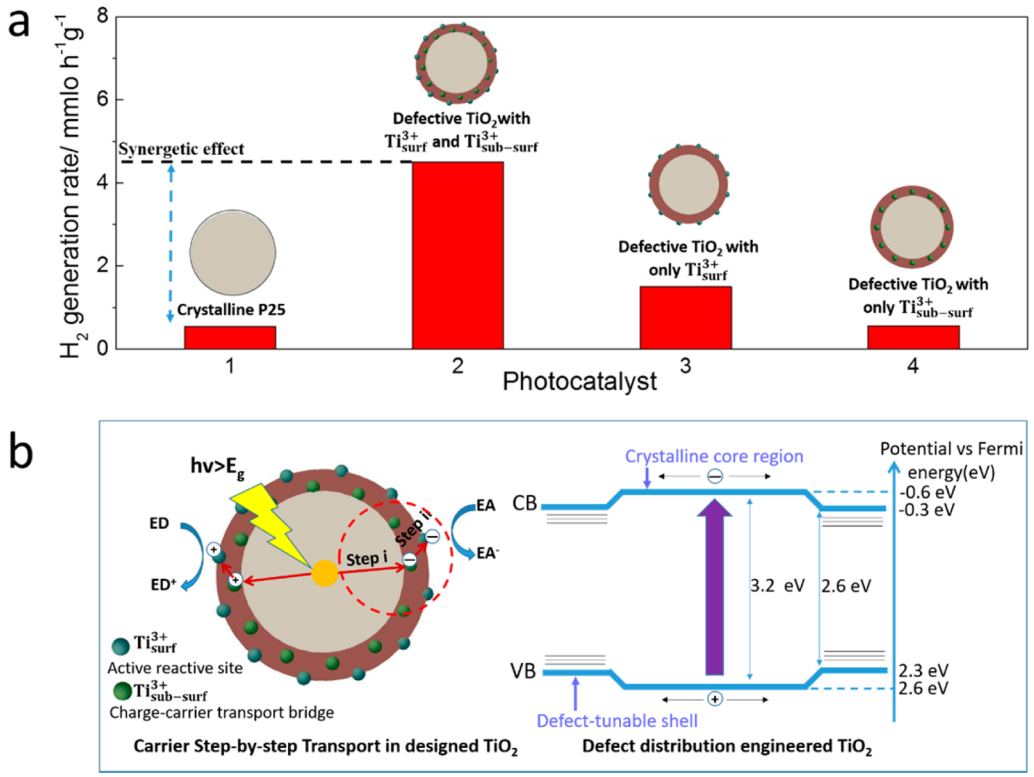

Figure 5. Photocatalytic performance and carrier transporting mechanism of designed TiO_2 compared with reference samples. (a) Comparisons of the average photocatalytic hydrogen generation rates of the designed defective TiO_2 with reference samples. (b) CST mechanism in designed TiO_2 with band alignment and shallow traps.

induce the synthesis of defective TiO_2. Therefore, the defective TiO_2 with the structure of a crystalline core@ both subsurface and surface defects doped shell has been successfully created based on the F-assisted synthesis method.

The defect induced element valence and energy band structure of prepared defective TiO_2 have been investigated. To give a qualitative interpretation of electrical states of the defective TiO_2, we performed electron energy loss spectrum (EELS), as shown in Figure 4a. For Ti L_2 and L_3 edge, the Ti 3d character splits into two groups: the 3-fold t_{2g} and the 2-fold e_g orbitals, owing to the octahedral coordination with O atom forming s-type and p-type bonds. The t_{2g}−e_g splitting in L_3 is 1.079 eV in prepared TiO_2, which is 39.3% narrower than 1.778 eV in P25. In the meantime, the t_{2g}−e_g splitting in L_2 is 1.143 eV in prepared TiO_2, which is 41.9% narrower than 1.963 eV in P25. The noteworthy difference observed for both the L_2 and L_3 peaks splitting can be attributed to the presence of Ti^{3+} in the prepared defective TiO_2.[7,27] Moreover, the high-resolution XPS Ti 2p spectrum of element Ti was conducted to clarify the Ti state (Figure S7). For crystalline P25, there are only two only peaks at about 458 and 464 nm representing Ti^{4+}, whereas there are another two peaks at 457.5 and 463.7 nm for prepared TiO_2, which indicates that there is Ti^{3+} in the synthesized TiO_2.[19,28] Furthermore, the presence of Ti^{3+} in the prepared TiO_2 was further investigated by electron paramagnetic resonance (EPR). The EPR spectra (Figure 4b) show that Ti^{3+}_{surf} and $Ti^{3+}_{sub-surf}$ are existing simultaneously in prepared TiO_2 because the anisotropic powder pattern g-values of $g_x = g_y = 1.978$ and $g_z = 1.946$ are obtained, which is caused by $Ti^{3+}_{sub-surf}$ in the disordered shell, whereas a weaker EPR signal observed at $g = 2.003$ assigned to Ti^{3+}_{surf} on the surface of TiO_2.[26] No obvious Ti^{3+} signal is seen for referenced Degussa P25. Hence, the defects in synthesized TiO_2 observed in Figure 3a can be attributed to Ti^{3+}_{surf} and $Ti^{3+}_{sub-surf}$. The existence of Ti^{3+}_{surf} and $Ti^{3+}_{sub-surf}$ defects in synthesized TiO_2 may induce the change of gap size and introduce intermediate midgap states,[29] which can lead to the significant variation of the energy band structure.

Hence, we have used the diffusive reflectance UV−vis spectroscopy (Figure 4c) to investigate the energy band structure of prepared TiO_2. The bandgap of the P25 is about 3.2 eV, whereas the UV onset of the prepared defective TiO_2 absorption occurred at ~2.6 eV which suggests that the optical gap of the prepared defective TiO_2 is substantially narrowed by intraband transitions. To further clarify the bandgap state of prepared TiO_2, X-ray photoelectron spectroscopy (XPS) is performed to provide useful information on the valence band (VB) position of prepared defective TiO_2, as shown in Figure 4d. The XPS VB spectrum shows there are many differences between P25 and defective TiO_2. P25 displays the characteristic VB density of states of TiO_2, with the band edge at 2.6 eV below the Fermi energy. Since the optical bandgap of P25 is 3.2 eV, the conduction band (CB) minimum would occur at 0.6 eV. However, XPS VB of our defective TiO_2 shows notable differences: the main absorption onset was located at 1.8 eV, whereas the maximum energy associated with the band tail blue-shifted further toward the vacuum level at about 0.8 eV. The change of the band structure in defective TiO_2 can be attributed the Ti^{3+}.

On the basis of the above results, it is demonstrated that defective TiO_2 has been synthesized with the unique crystal and band structure. Combining the characterization results and recent study on defective TiO_2,[30] the structure and the density of state for P25 and our defective TiO_2 can be clearly described as Figure 4e. Both representations were built using

DOI: 10.1021/acsami.6b14700
ACS Appl. Mater. Interfaces 2017, 9, 4634−4642

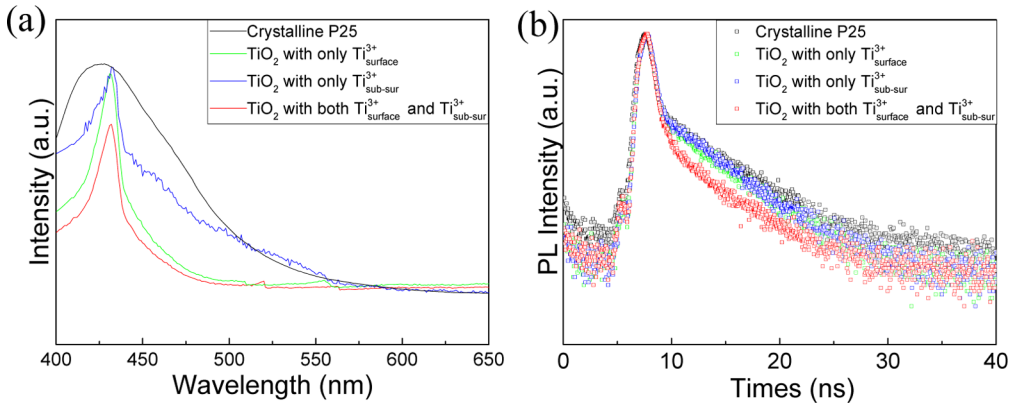

Figure 6. Carrier transport kinetics of defective TiO_2. (a) Photoluminescence spectra and (b) photoluminescence decay profiles.

experimental data from UV−vis spectroscopy and XPS analysis when the energy positions of V_O localized states are referred from the reported works.[17,21,23] For prepared defective TiO_2, $Ti^{3+}_{sub-surf}$ defects are in the tailored disordered shell and Ti^{3+}_{surf} on the surface of the shell, whereas there is no Ti^{3+} in the crystalline P25. Compared with the big bandgap of 3.2 eV in P25 with the conduction band (CB) minimum at −0.7 eV and the valence band (VB) maximum at 2.5 eV, our defective TiO_2 shows narrow bandgap of 2.6 eV with the conduction band (CB) minimum at −0.4 eV and the valence band (VB) maximum at 2.2 eV. The 0.3 eV lower of CB and 0.3 eV higher of VB can result in the special band matching that both electrons and holes can easily transport from bulk to surface. In addition, the localized band states introduced by Ti^{3+} related oxygen vacancy (V_O) sates are always reported to be 0.7−1.0 eV below the CB minimum of defective TiO_2.[26,27,31] This crystal and band structure of synthesized TiO_2 is consistent with our design structure for incorporating the CST into TiO_2.

Although we have acquired the expected crystal and band structure in designed TiO_2 (Figure 4), it remains to see whether this structure can really initiate CST for efficient photocatalytic hydrogen generation. Therefore, we have carried out the photocatalytic hydrogen generation evolution. As shown in Figure 5a, designed TiO_2 ($R_{F\text{-}4}$) with both Ti^{3+}_{surf} and $Ti^{3+}_{sub-surf}$ demonstrates a significantly improved photocatalytic activity in hydrogen evolution compared with the other three reference TiO_2 samples: crystalline P25, prepared TiO_2 with only Ti^{3+}_{surf}, and prepared TiO_2 with only $Ti^{3+}_{sub-surf}$ (the characterization of Ti^{3+} by EPR and the absorption spectra of these two prepared defective TiO_2 can be seen in Figure S8, the diffusive reflectance UV−vis spectra can be seen in Figure S9, the HRTEM images of TiO_2 with only Ti^{3+}_{surf} and only $Ti^{3+}_{subsurf}$ can be seen in Figure S10). Since all the TiO_2 samples used for comparison have the similar morphology and similar size about 25 nm, the distinct difference in photocatalytic performance among defective TiO_2 ($R_{F\text{-}4}$) and other samples can be attributed to the moderate $Ti^{3+}_{sub-surf}$ and abundant Ti^{3+}_{surf} concentration in $R_{F\text{-}4}$. Obviously, $R_{F\text{-}4}$ shows the best average hydrogen evolution rate up to 4.21 mmol h^{-1} g^{-1}, which is much better than 0.54 mmol h^{-1} g^{-1} for P25. In addition, TiO_2 with only Ti^{3+}_{surf} can show much enhanced photocatalytic performance than P25 while TiO_2 with only $Ti^{3+}_{sub-surf}$ shows similar performance compared with P25, because Ti^{3+}_{surf} can act as the reactive reaction sites to enhance photocatalysis while $Ti^{3+}_{sub-surf}$ acts as both the carrier transport bridge and recombination center. Furthermore, the better performance of $R_{F\text{-}4}$ than TiO_2 with only Ti^{3+}_{surf} can be attributed to the positive function of $Ti^{3+}_{sub-surf}$ by bridging the carriers to the surface of TiO_2, because the two samples have a similar Ti^{3+}_{surf} concentration.

On the basis of the experimental phenomena and the reported role of Ti^{3+} defects,[30,32] the CST mechanism in designed TiO_2 can be clearly described in Figure 5b. In designed TiO_2, carriers can be trapped by the $Ti^{3+}_{sub-surf}$ defects first and then transferred to the Ti^{3+}_{surf} step by step, which is a CST with proper band alignment, shallow traps and active surface sites. In CST, moderate concentration of subsurface defects ($Ti^{3+}_{sub-surf}$) play the role as the carriers transport bridge and abundant surface Ti^{3+} defects (Ti^{3+}_{surf}) act as both carriers acceptors and active reactive sites. Hence, the CST can effectively promote the carrier transport for efficient photocatalytic hydrogen generation.

Considering the wide bang-gap of defective TiO_2 ($R_{F\text{-}4}$), we have investigated the effects of its broad absorbance on the hydrogen generation performance. The apparent quantum efficiency (AQE) is calculated referring to some reported works,[33−35] and the AQE of platinized defective TiO_2 ($R_{F\text{-}4}$) is up to 25.1% at 380 nm and drops to 3.5% at 420 nm. The hydrogen generation performance of $R_{F\text{-}4}$ is conducted under visible light (400 nm<λ<780 nm) and shows 580 μmol h^{-1} g^{-1}, much less than the 4.21 mmol h^{-1} g^{-1} under ultraviolet light, corresponding to the AQE results. As a control, to exclude the effects of light absorbance on the CST, the EIS spectra of these four samples without light irradiation is performed (as shown in Figure S11), which are consistent with the photocatalysis performance of samples in Figure 5a. This further supports that the CST is efficient in transporting carriers and that such a transmission is originated from the prepared unique defective structure rather than the wide light absorbance.

The intrinsic charge-carrier separation and transport efficiency of TiO_2 samples have been investigated through photoluminescence (PL) spectra and PL emission decay profiles, which are effective to reveal the kinetics of carrier dynamics.[2,9] As shown in Figure 6a, the TiO_2 ($R_{F\text{-}4}$) with both Ti^{3+}_{surf} and $Ti^{3+}_{sub-surf}$ can show the lowest PL intensity compared other samples, suggesting that the introduced defects could greatly improve the separation and transportation of charge carriers.

Furthermore, the more powerful evidence for investigating the charge-carrier separation and transportation kinetics is provided by PL emission decay profiles (Figure 6b). The PL emission decay profiles of all of the samples could be expressed

DOI: 10.1021/acsami.6b14700
ACS Appl. Mater. Interfaces 2017, 9, 4634−4642

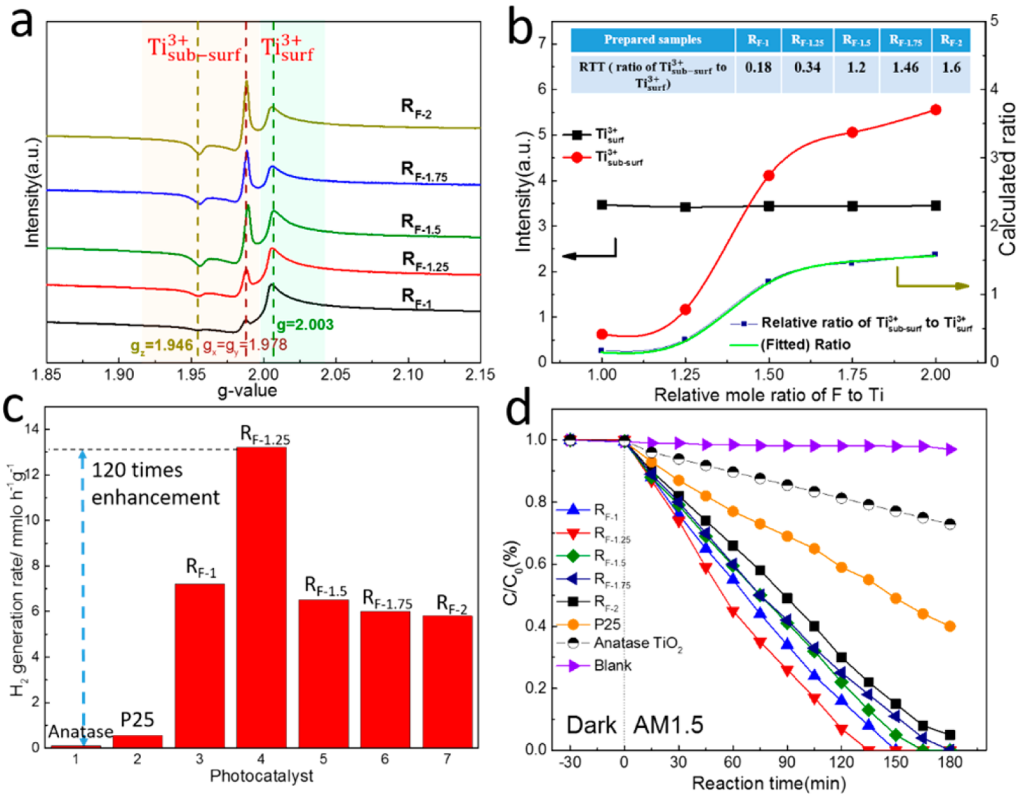

Figure 7. Defective TiO_2 with the tunable RTT and their performance on photocatalytic degradation and hydrogen generation. (a) EPR *g* values of samples with different ratios of F:Ti. (b) Correlation of the signal area obtained from double integration of the Ti^{3+} signals of the samples. (c, d) Photocatalytic degradation of methyl orange and hydrogen generation performance for samples with different Ti^{3+} DD.

by biexponential fitting, indicating that PL decay occurred through two relaxation pathways. Table S1 summarizes the PL lifetimes and fractional intensities of samples which shows that the amplitude-weighted average lifetimes (τ_{ave}) of TiO_2 with both Ti^{3+}_{surf} and $Ti^{3+}_{subsurf}$ is 2.09 ns, much lower than TiO_2 with only Ti^{3+}_{surf} (3.07 ns) and TiO_2 with only $Ti^{3+}_{subsurf}$ (2.99 ns), and P25 (3.26 ns). Since the lower τ_{ave} indicates the faster carrier transport,[9] it can be concluded that the TiO_2 with Ti^{3+}_{surf} and $Ti^{3+}_{subsurf}$ can show the best charge transporting efficiency, proving that the CST really plays an active role in enhancing the carrier transporting kinetics.

Because the efficient carrier transport to the surface can greatly enhance the photocatalysis, it is feasible to achieve much better photocatalytic performance through further promoting the kinetics of CST. In addition to acting as the transport bridge of carriers, the defect induced traps can also act as the recombination center. The relationship between this recombination rate (k_{rec}) and the separation distance of carriers (R_{sep}) can be described as follows:[36]

$$k_{rec} \propto \exp(-2R_{sep}/a_0)$$

where a_0 is the radius of the hydrogenlike wave equation for capturing carriers. On the one hand, when the concentration of subsurface defects is relatively low, the CST will not be efficient enough due to the insufficient capacity of capturing carriers as many as possible. On the other hand, when there are too many subsurface defects, the R_{sep} will be shorter and thus the k_{rec} will rise. Hence, there must be the optimal concentration of subsurface defects. Combined with the role of surface defects which can act as the active sites to accept the carriers transferred from the subsurface defects, there must be an optimal ratio of subsurface defects to surface defects for efficient CST.

Hence, for our designed TiO_2, we have considered more precisely tailoring the ratio of $Ti^{3+}_{sub-surf}$ to Ti^{3+}_{surf} (such a ratio is defined as RTT) to further promote the kinetics of CST for efficient photocatalysis. On the basis of the aforementioned fluorine-assisted dynamic solvothermal method, the samples with the tunable RTT have been synthesized by adjusting the raw material mole ratio of F:Ti from 1 to 2 precisely, and the concentration of $Ti^{3+}_{sub-surf}$ and Ti^{3+}_{surf} changes respectively as shown in Figure 7a. Importantly, the XRD spectra (Figure S12) and SEM images (the insets in Figure S12 indicate that the samples have nearly the same morphology and crystal structure. Furthermore, we have calculated the amount of $Ti^{3+}_{sub-surf}$ and Ti^{3+}_{surf}, respectively, and worked out the precise RTT (Figure 7b) based on the signal area obtained from double integration of $Ti^{3+}_{sub-surf}$ and Ti^{3+}_{surf}signal. When the relative mole ratio of F: Ti is 1.0 (R_{F-1}), the Ti^{3+}_{surf} signal is strong while there is a very weak $Ti^{3+}_{sub-surf}$ signal. As the relative mole ratio of F: Ti increases, the Ti^{3+}_{surf} signal keeps stable, whereas the $Ti^{3+}_{sub-surf}$ signal becomes stronger. When the mole ratio of F:Ti increases from 1.0 to 2.0, the samples R_{F-1}, $R_{F-1.25}$, $R_{F-1.5}$, $R_{F-1.75}$, R_{F-2} show the corresponding RTT 0.18, 0.34, 1.20, 1.46, and 1.60, respectively.

As shown in Figure 7c, photocatalytic hydrogen generation performance of prepared defective TiO_2 with tunable RTT from 0.18 to 1.6, commercial P25 and commercial crystalline anatase TiO_2 (all the TiO_2 samples used for comparison have the similar morphology and similar size about 25 nm) reveals that all our prepared samples show better performance than P25 and crystalline anatase TiO_2. As the RTT in TiO_2

DOI: 10.1021/acsami.6b14700
ACS Appl. Mater. Interfaces 2017, 9, 4634−4642

decreases from 1.6 (R_{F-2}) to 0.34 ($R_{F-1.25}$), our defective TiO_2 samples show better performance progressively while the prepared sample R_{F-1} with the RRT 0.18 shows the worse performance than $R_{F-1.25}$. The sample $R_{F-1.25}$ shows the state-of-the-art activity among anatase TiO_2 for sunlight-driven photocatalytic hydrogen generation up to 13.21 mmol h^{-1} g^{-1}, which is 120 times enhancement than 0.11 mmol h^{-1} g^{-1} for the crystalline anatase TiO_2. Actually, R_{F-4} and R_{F-6} shows a little worse photocatalytic performance than R_{F-2}: 4.21 mmol h^{-1} g^{-1} for R_{F-4} for and 4 mmol h^{-1} g^{-1} for R_{F-6}, which are a little worse than 5.8 mmol h^{-1} g^{-1} for R_{F-2}. The photocatalytic degradation of methyl orange (as shown in Figure 7d) shows the results consistent with the photocatalytic hydrogen generation. The TiO_2 with relatively low RTT can show better photocatalytic degradation performance and the optimal is 0.34, which shows the best degradation performance finishing degrading the MO in 130 min under AM 1.5. Hence, the relatively lower RTT is better for photocatalytic hydrogen generation and photocatalytic degradation and the optimal RTT is 0.34. The EIS of the samples (Figure S13) also indicate that defective TiO_2 with RTT 0.34 can show the best carriers conductivity. Therefore, it is efficient to lower the RTT to promote the CST kinetics for efficient photocatalysis and the optimal RTT is 0.34.

4. CONCLUSION

In summary, the CST can enable typical semiconductor TiO_2 to show excellent photocatalytic hydrogen generation performance. By tailoring defect distribution to create a crystalline core/defect-tunable shell structure through fluorine-induced dynamic reaction method, there are suitable band alignment, moderate bridgelike shallow traps and active carrier acceptors in TiO_2, which initiate the CST. It is demonstrated that the designed TiO_2 with the CST can exhibit high performance in photocatalytic hydrogen generation: designed TiO_2 with the optimal ratio (0.34) of subsurface to surface defects can show the state-of-the-art activity among anatase TiO_2 for sunlight-driven photocatalytic hydrogen generation from water splitting up to 13.21 mmol h^{-1} g^{-1}, which is 120 times enhanced than the crystalline anatase TiO_2. The enhancement is attributed to the efficient CST originating from engineered defects in designed TiO_2. The finding of this work proves that the CST enabled by defect engineering can be used to significantly improve photocatalytic hydrogen generation performance in semiconductor photocatalysts.

■ ASSOCIATED CONTENT

Supporting Information

The Supporting Information is available free of charge on the ACS Publications website at DOI: 10.1021/acsami.6b14700.

Detailed forming mechanism research of defective TiO_2, relevant XRD, EPR, TEM, EIS, XPS, and the comparison table of the photocatalytic hydrogen production (PDF)

■ AUTHOR INFORMATION

Corresponding Author

*E-mail: mcli@ncepu.edu.cn. Fax: +86 10 6177 2951. Tel: +86 10 6177 2951.

ORCID

Hong Liu: 0000-0003-1640-9620

Notes

The authors declare no competing financial interest.

■ ACKNOWLEDGMENTS

This work is supported partially by National High-tech R&D Program of China (863 Program, No. 2015AA034601), National Natural Science Foundation of China (Grant nos. 91333122, 51372082, 51402106 and 11504107), Ph.D. Programs Foundation of Ministry of Education of China (Grant nos. 20130036110012), Par-Eu Scholars Program, Beijing Municipal Science and Technology Project (Z161100002616039), and the Fundamental Research Funds for the Central Universities (2016JQ01, 2015ZZD03, 2015ZD07).

■ REFERENCES

(1) Zhang, N.; Li, X.; Ye, H.; Chen, S.; Ju, H.; Liu, D.; Lin, Y.; Ye, W.; Wang, C.; Xu, Q.; et al. Oxide Defect Engineering Enables to Couple Solar Energy into Oxygen Activation. *J. Am. Chem. Soc.* **2016**, *138*, 8928−8935.

(2) Schneider, J.; Matsuoka, M.; Takeuchi, M.; Zhang, J.; Horiuchi, Y.; Anpo, M.; Bahnemann, D. W. Understanding TiO_2 Photocatalysis: Mechanisms and Materials. *Chem. Rev.* **2014**, *114*, 9919−9986.

(3) Liu, M.; Chen, Y.; Su, J.; Shi, J.; Wang, X.; Guo, L. Photocatalytic Hydrogen Production using Twinned Nanocrystals and an Unanchored NiS_x Co-catalyst. *Nature Energy* **2016**, *1*, 16151.

(4) Liu, X.; Iocozzia, J.; Wang, Y.; Cui, X.; Chen, Y.; Zhao, S.; Li, Z.; Lin, Z. Noble Metal-metal Oxide Nanohybrids with Tailored Nanostructures for Efficient Solar Energy Conversion, Photocatalysis and Environmental Remediation. *Energy Environ. Sci.* **2017**, DOI: 10.1039/C6EE02265K.

(5) Wu, Q.; Huang, F.; Zhao, M.; Xu, J.; Zhou, J.; Wang, Y. Ultrasmall Yellow Defective TiO_2 Nanoparticles for Co-catalyst Free Photocatalytic Hydrogen Production. *Nano Energy* **2016**, *24*, 63−71.

(6) Chen, X.; Liu, L.; Yu, P. Y.; Mao, S. S. Increasing Solar Absorption for Photocatalysis with Black Hydrogenated Titanium Dioxide Nanocrystals. *Science* **2011**, *331*, 746−750.

(7) Li, L.; Yan, J.; Wang, T.; Zhao, Z. J.; Zhang, J.; Gong, J.; Guan, N. Sub-10 nm Rutile Titanium Dioxide Nanoparticles for Efficient Visible-light-driven Photocatalytic Hydrogen Production. *Nat. Commun.* **2015**, *6*, 5881.

(8) Yang, Y.; Liu, G.; Irvine, J. T.; Cheng, H. M. Enhanced Photocatalytic H_2 Production in Core-Shell Engineered Rutile TiO_2. *Adv. Mater.* **2016**, *28*, 5850−5856.

(9) Zhang, K.; Wang, L.; Kim, J. K.; Ma, M.; Veerappan, G.; Lee, C.-L.; Kong, K.-j.; Lee, H.; Park, J. H. An Order/Disorder/Water Junction System for Highly Efficient Co-catalyst-free Photocatalytic Hydrogen Generation. *Energy Environ. Sci.* **2016**, *9*, 499−503.

(10) Fazio, G.; Ferrighi, L.; Di Valentin, C. Photoexcited Carriers Recombination and Trapping in Spherical vs Faceted TiO_2 Nanoparticles. *Nano Energy* **2016**, *27*, 673−689.

(11) Li, J.; Wu, N. Semiconductor-based Photocatalysts and Photoelectrochemical Cells for Solar Fuel Generation: a Review. *Catal. Sci. Technol.* **2015**, *5*, 1360−1384.

(12) Wang, X.; Long, R.; Liu, D.; Yang, D.; Wang, C.; Xiong, Y. Enhanced Full-spectrum Water Splitting by Confining Plasmonic Au Nanoparticles in N-doped TiO_2 Bowl Nanoarrays. *Nano Energy* **2016**, *24*, 87−93.

(13) Liu, G.; Yin, L.-C.; Wang, J.; Niu, P.; Zhen, C.; Xie, Y.; Cheng, H.-M. A Red Anatase TiO_2 Photocatalyst for Solar Energy Conversion. *Energy Environ. Sci.* **2012**, *5*, 9603−9610.

(14) Pan, X.; Yang, M.-Q.; Fu, X.; Zhang, N.; Xu, Y.-J. Defective TiO_2 with Oxygen Vacancies: Synthesis, Properties and Photocatalytic Applications. *Nanoscale* **2013**, *5*, 3601−3614.

(15) Minella, M.; Faga, M. G.; Maurino, V.; Minero, C.; Pelizzetti, E.; Coluccia, S.; Martra, G. Effect of Fluorination on the Surface

DOI: 10.1021/acsami.6b14700
ACS Appl. Mater. Interfaces 2017, 9, 4634−4642

Properties of Titania P25 Powder: an FTIR Study. *Langmuir* **2010**, *26*, 2521−2527.
(16) Gordon, T. R.; Cargnello, M.; Paik, T.; Mangolini, F.; Weber, R. T.; Fornasiero, P.; Murray, C. B. Nonaqueous Synthesis of TiO_2 Nanocrystals Using TiF_4 to Engineer Morphology, Oxygen Vacancy Concentration, and Photocatalytic Activity. *J. Am. Chem. Soc.* **2012**, *134*, 6751−6761.
(17) Liu, N.; Schneider, C.; Freitag, D.; Hartmann, M.; Venkatesan, U.; Müller, J.; Spiecker, E.; Schmuki, P. Black TiO_2 Nanotubes: Cocatalyst-free Open-circuit Hydrogen Generation. *Nano Lett.* **2014**, *14*, 3309−3313.
(18) Tian, M.; Mahjourisamani, M.; Eres, G.; Sachan, R.; Yoon, M.; Chisholm, M. F.; Wang, K.; Puretzky, A. A.; Rouleau, C. M.; Geohegan, D. B.; Duscher, G. Structure and Formation Mechanism of Black TiO_2 Nanoparticles. *ACS Nano* **2015**, *9*, 10482−10488.
(19) Cui, H.; Zhao, W.; Yang, C.; Yin, H.; Lin, T.; Shan, Y.; Xie, Y.; Gu, H.; Huang, F. Black TiO_2 Nanotube Arrays for High-efficiency Photoelectrochemical Water-splitting. *J. Mater. Chem. A* **2014**, *2*, 8612−8616.
(20) Wang, Z.; Yang, C.; Lin, T.; Yin, H.; Chen, P.; Wan, D.; Xu, F.; Huang, F.; Lin, J.; Xie, X.; Jiang, M. Visible-light Photocatalytic, Solar Thermal and Photoelectrochemical Properties of Aluminium-reduced Black Titania. *Energy Environ. Sci.* **2013**, *6*, 3007−3014.
(21) Wang, Z.; Yang, C.; Lin, T.; Yin, H.; Chen, P.; Wan, D.; Xu, F.; Huang, F.; Lin, J.; Xie, X.; Jiang, M. H-Doped Black Titania with Very High Solar Absorption and Excellent Photocatalysis Enhanced by Localized Surface Plasmon Resonance. *Adv. Funct. Mater.* **2013**, *23*, 5444−5450.
(22) Xu, C.; Song, Y.; Lu, L.; Cheng, C.; Liu, D.; Fang, X.; Chen, X.; Zhu, X.; Li, D. Electrochemically Hydrogenated TiO_2 Nanotubes with Improved Photoelectrochemical Water Splitting Performance. *Nanoscale Res. Lett.* **2013**, *8*, 391.
(23) Yu, J. C.; Yu, J.; Ho, W.; Jiang, Z.; Zhang, L. Effects of F^- Doping on the Photocatalytic Activity and Microstructures of Nanocrystalline TiO_2 Powders. *Chem. Mater.* **2002**, *14*, 3808−3816.
(24) Czoska, A.; Livraghi, S.; Chiesa, M.; Giamello, E.; Agnoli, S.; Granozzi, G.; Finazzi, E.; Valentin, C. D.; Pacchioni, G. The Nature of Defects in Fluorine-doped TiO_2. *J. Phys. Chem. C* **2008**, *112*, 8951−8956.
(25) Gordon, T. R.; Cargnello, M.; Paik, T.; Mangolini, F.; Weber, R. T.; Fornasiero, P.; Murray, C. B. Nonaqueous Synthesis of TiO_2 Nanocrystals using TiF_4 to Engineer Morphology, Ooxygen Vacancy Concentration, and Photocatalytic Activity. *J. Am. Chem. Soc.* **2012**, *134*, 6751−6761.
(26) Zuo, F.; Wang, L.; Wu, T.; Zhang, Z. Y.; Borchardt, D.; Feng, P. Y. Self-Doped Ti^{3+} Enhanced Photocatalyst for Hydrogen Production under Visible Light. *J. Am. Chem. Soc.* **2010**, *132*, 11856−11857.
(27) Naldoni, A.; Allieta, M.; Santangelo, S.; Marelli, M.; Fabbri, F.; Cappelli, S.; Bianchi, C. L.; Psaro, R.; Dal Santo, V. Effect of Nature and Location of Defects on Bandgap Narrowing in Black TiO_2 Nanoparticles. *J. Am. Chem. Soc.* **2012**, *134*, 7600−7603.
(28) Chen, J.; Song, W.; Hou, H.; Zhang, Y.; Jing, M.; Jia, X.; Ji, X. Ti^{3+} Self-Doped Dark Rutile TiO_2 Ultrafine Nanorods with Durable High-Rate Capability for Lithium-Ion Batteries. *Adv. Funct. Mater.* **2015**, *25*, 6793−6801.
(29) Wang, Z.; Wen, B.; Hao, Q.; Liu, L. M.; Zhou, C.; Mao, X.; Lang, X.; Yin, W. J.; Dai, D.; Selloni, A.; Yang, X. Localized Excitation of Ti^{3+} Ions in the Photoabsorption and Photocatalytic Activity of Reduced Rutile TiO_2. *J. Am. Chem. Soc.* **2015**, *137*, 9146−9152.
(30) Liu, L.; Chen, X. Titanium Dioxide Nanomaterials: Self-structural Modifications. *Chem. Rev.* **2014**, *114*, 9890−9918.
(31) Finazzi, E.; Di Valentin, C.; Pacchioni, G.; Selloni, A. Excess Electron States in Reduced Bulk Anatase TiO_2: Comparison of Standard GGA, GGA+U, and Hybrid DFT Calculations. *J. Chem. Phys.* **2008**, *129*, 154113−154119.
(32) Asahi, R.; Morikawa, T.; Irie, H.; Ohwaki, T. Nitrogen-doped Titanium Dioxide as Visible-light-sensitive Photocatalyst: Designs, Developments, and Prospects. *Chem. Rev.* **2014**, *114*, 9824−9852.
(33) Zuo, F.; Wang, L.; Wu, T.; Zhang, Z.; Borchardt, D.; Feng, P. Self-doped Ti^{3+} Enhanced Photocatalyst for Hydrogen Production under Visible Light. *J. Am. Chem. Soc.* **2010**, *132*, 11856−11857.
(34) Yang, M.-Q.; Han, C.; Xu, Y.-J. Insight into the Effect of Highly Dispersed MoS_2 versus Layer-Structured MoS_2 on the Photocorrosion and Photoactivity of CdS in Graphene−CdS−MoS_2 Composites. *J. Phys. Chem. C* **2015**, *119*, 27234−27246.
(35) Yuan, L.; Han, C.; Yang, M.-Q.; Xu, Y.-J. Photocatalytic Water Splitting for Solar Hydrogen Generation: Fundamentals and Recent Advancements. *Int. Rev. Phys. Chem.* **2016**, *35*, 1−36.
(36) Zhu, Y.; Yao, W.; Zong, R. *Photocatalysis: Application on Environmental Purification and Green Energy*; Chemical Industry Press: Beijing, 2015; p 13.

DOI: 10.1021/acsami.6b14700
ACS Appl. Mater. Interfaces 2017, 9, 4634−4642